Numerical and experimental investigation of buoyancy-driven dissolution in vertical fracture

C. Oltean, F. Golfier, M. A. Bues

JOURNAL OF GEOPHYSICAL RESEARCH: SOLID EARTH, VOL. 118, 2038–2048, doi:10.1002/jgrb.50188, 2013

Numerical and experimental investigation of buoyancy-driven dissolution in vertical fracture

Constantin Oltéan,[1] Fabrice Golfier,[1] and Michel Antoine Buès[1]

Received 21 December 2012; revised 12 April 2013; accepted 14 April 2013; published 22 May 2013.

[1] Alteration and dissolution resulting from reactive fluid flows in vertical fracture are investigated from numerical and laboratory experiments. Due to fluid density contrast, buoyancy effects are observed leading to significant changes in fracture geometry. Buoyant and forced convection forces act here in the same direction. The experiments were carried out at two different flow rates. When buoyancy forces are preponderant (low injection flow rate), the dissolution rate increases with the vertical distance. By contrast, for convection-dominated transport (high injection flow rate), a uniform dissolution is observed. Using numerical simulations, four dissolution regimes were identified. The fracture patterns observed strongly depend on the characteristic dimensionless numbers of the process, respectively, the Richardson, Damköhler, and Péclet numbers. The good agreement between numerical simulations and experimental results in terms of fracture patterns highlights the capability of the numerical model to describe the complex coupling between flow dynamics, buoyancy, and chemical reaction. Finally, a 3-D behavior diagram is constructed to illustrate these interactions and as a means of relating the appropriate dimensionless parameters to the morphological changes observed.

Citation: Oltéan, C., F. Golfier, and M. A. Buès (2013), Numerical and experimental investigation of buoyancy-driven dissolution in vertical fracture, *J. Geophys. Res. Solid Earth*, *118*, 2038–2048, doi:10.1002/jgrb.50188.

1. Introduction

[2] Mineral dissolution occurring during fluid flow in fractures—especially if halite or carbonate minerals are present—may significantly affect the groundwater chemistry and the hydrodynamic behavior of the large-scale porous formations. This issue is a great concern for many subsurface applications. The genesis of karst systems, dam stability, salt mining, or geological CO2 storage and leakage are only a few examples among the most crucial ones. As noted in the literature [*Berkowitz and Zhou*, 1996; *Békri et al*., 1997; *Dijk and Berkowitz*, 1998; *Berkowitz*, 2002; *Dijk et al*., 2002; *Golfier et al*., 2002; *Detwiler et al*., 2003; *Detwiler*, 2008; *Szymczak and Ladd*, 2009, 2012], the dissolution phenomenon is a complex process mainly driven by the fluid velocity, the diffusion of dissolved compounds, and the kinetics of geochemical reactions occurring at the rock surface. When fluid flow is the only driving force (i.e., no buoyancy effect), numerical and experimental investigations [e.g., *Békri et al*., 1997; *Kang et al*., 2003; *Detwiler and Rajaram*, 2007] have shown that the evolution of the fracture pattern can be described through two dimensionless numbers: the Péclet (*Pe*) and the Damköhler (*Da*) numbers.

[3] However, in most of the applications of interest, the dependency of the dissolution on the variation in fluid properties (density and/or viscosity) cannot be disregarded [*Anderson and Kirkland*, 1980; *Weisbrod et al*., 2012]. Due to the solubility of dissolved minerals, chemical changes in fluid composition are expected which may generate the kind of instabilities classically observed between two miscible fluids with density contrast [e.g., *Wooding et al*., 1997; *Simmons et al*., 2002; *Mainhagu et al*., 2012]. Recent experimental studies carried out by *Dijk and Berkowitz* [2000] or *Dijk et al*. [2002] confirm this hypothesis. Using a plane-rough fracture made from a block of natural halite, these authors showed that, when the fracture is oriented horizontally and is subjected to high *Da* numbers, the lower fracture wall dissolves less rapidly than the upper one. For low *Da* numbers, uniform dissolution at a constant rate of both walls is observed. In a similar way, upward flow through a vertical fracture induces, at high *Da* numbers, a more rapid dissolution of the upper part of the sample. These observations evidently suggest that, under buoyancy effects, the dissolution pattern depends not only on the *Pe* and *Da* numbers but also on the orientation and elevation of the fracture walls [*Dijk et al*., 2002; *Berkowitz*, 2002]. The numerical investigation by *Chaudhuri et al*. [2009] of buoyancy-driven dissolution in vertical limestone fractures supports this analysis. A modified critical Rayleigh (*Ra*) number is proposed to characterize the onset of instabilities. Similar numerical evidence is also observed by *Luo et al*. [2012] for a plane fracture. A complex interaction between natural convection instabilities and roughness of dissolved walls emerges from the competition between Rayleigh and Péclet numbers.

[1]Université de Lorraine/CNRS/CREGU, UMR 7359 GeoRessources Laboratory, Vandœuvre-lès-Nancy, France.

Corresponding author: C. Oltéan, Université de Lorraine/CNRS/CREGU, UMR 7359 GeoRessources Laboratory, 2 Rue du Doyen Marcel Roubault, TSA 70605, 54518 Vandœuvre-lès-Nancy, France. (constantin.oltean@univ-lorraine.fr)

2169-9313/13/10.1002/jgrb.50188

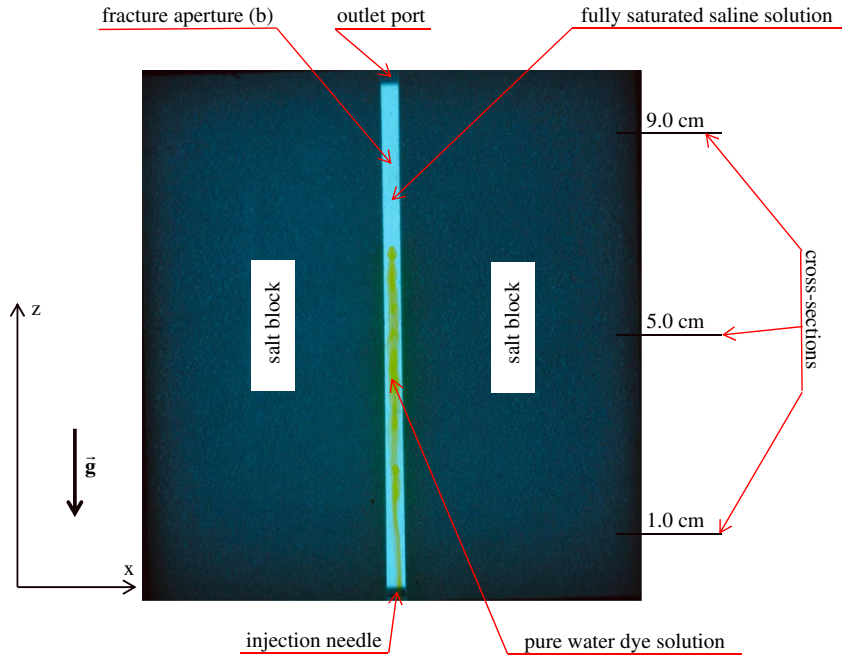

Figure 1. Experimental set-up.

[4] Nevertheless, comparative numerical and experimental studies are, to our knowledge, still inexistent and available experimental data are rare and—at best—incomplete. Moreover, it is still unclear to predict (1) what kind of dissolution patterns can be expected and (2) how these ones can be related to flow conditions and surface reaction kinetics. This critical issue remains an open question, as pointed out by *Berkowitz* [2002] in his review on flow and transport in fractured media. This paper aims at addressing this lack and proposing a preliminary diagram of dissolution regimes. For this purpose, upward injection through a vertically-oriented fracture is studied both experimentally and numerically for different fluid flow rates, reaction rates, and fluid density contrasts. Here, solutal buoyancy and forced convection forces act in the same direction. A plane vertical 2-D fracture has been built up to validate numerical simulations. Local variations in fracture aperture were followed across time using a CCD camera. The numerical model of coupled flow and dissolution processes is based on an Arbitrary Lagrangian Eulerian (ALE) method whose capability for simulating fluid-structure interactions has been demonstrated in the past [e.g., *Van Noorden*, 2009]. Based on this comparison, we discuss the impact of buoyancy on alteration patterns observed and a dissolution regime diagram is presented.

2. Material and Methods

[5] The experimental device is represented in Figure 1. The fracture is made of two compacted salt blocks (99.99% sodium chloride) of size $9.90 \times 3.50 \times 0.42$ cm, spaced about 0.3 cm apart. After sizing and polishing, the salt blocks were inserted between two parallel transparent glass plates supported by a rigid steel structure. During the mounting process, a maximal aperture variation of about 0.04 cm was observed. Rubber gaskets ensured a perfect sealing of the flow chamber. Then, the vertically-oriented cell is initially filled with a fully saturated brine solution ($C_{sat} = 357$ g/L) for 12 h until complete saturation of the porous medium. At this point, an undersaturated solution ($C_{inj} = 0$ g/L) is injected upward from a plastic injection needle. The injection needle (0.15 cm inner diameter) is centered between the two plates and located 0.25 cm above the lower cell edge. The fluid percolates through the fracture and induces dissolution of the walls before flowing out through the outlet port. A peristaltic pump ensures a quasi-constant flow rate. Measurements were performed for flow

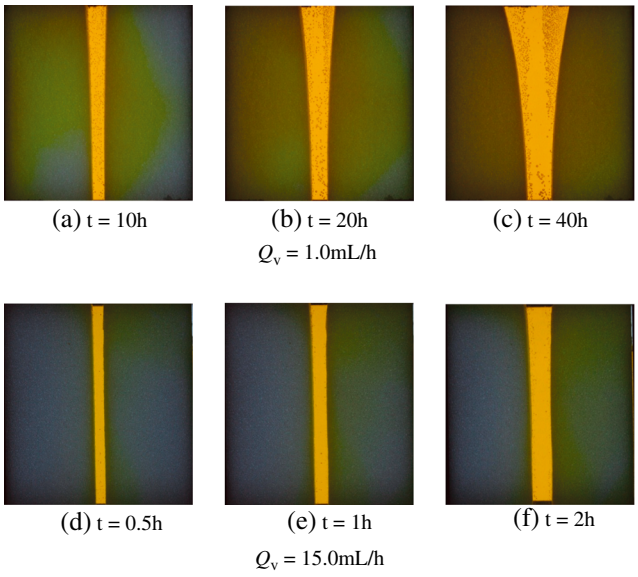

Figure 2. Change of the fracture aperture versus time for two injection flow rates (Q_v): (a)–(c) $Q_v = 1.0$ mL/h; (d)–(f) $Q_v = 15.0$ mL/h.

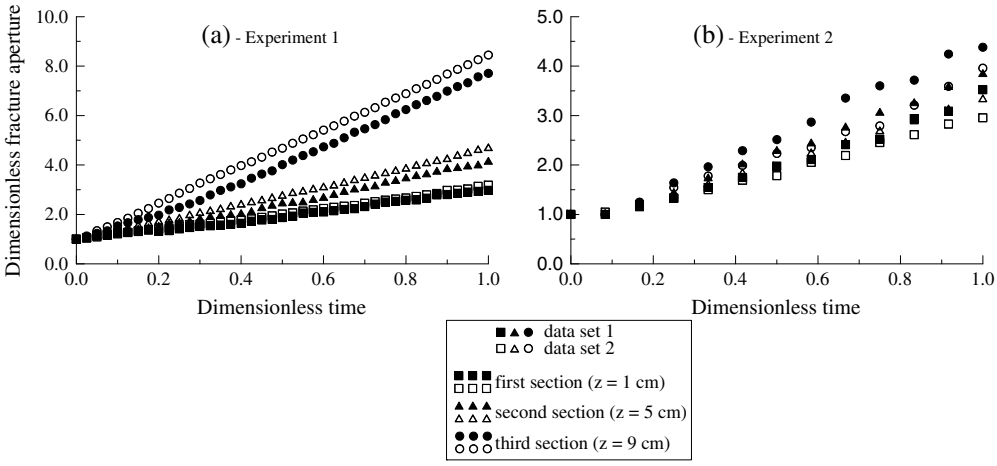

Figure 3. Evolution of the dimensionless fracture aperture versus time along three sections perpendicular to the mean flow for: (a) $Q_v = 1.0$ mL/h and (b) $Q_v = 15$ mL/h.

rates ranging from 1.0 to 15 mL/h. In order to better visualize the dissolution of salt blocks, the injected fluid was dyed with a few milligrams of fluorescein. Note that no significant dye leakage through the porous blocks has been detected during the duration of the experiments. The permeability measurement of salt blocks ($K_{matrix} = 4.5 \times 10^{-13}$ m^2) compared to the effective permeability of fracture ($K_{fracture} = 7.5 \times 10^{-7}$ m^2) confirms this observation. This negligible percolation rate and the high reaction rate of halite [*Alkattan et al*., 1997; *Weisbrod et al*., 2012] indicate that dissolution is limited by mass transfer. A high exchange mass coefficient between the fluid and porous phase is recovered and results in a sharp dissolving interface (local equilibrium solution) [*Hoefner and Fogler*, 1988; *Fredd and Miller*, 2000; *Golfier et al*., 2002] equivalent to the dissolution process of a solid phase if the diffuse layer is thin enough. This approach has been used by *Luo et al*. [2012] where the solid phase was represented as a porous medium with very low porosity and permeability. We adopt the same assumption here and will consider that fracture walls are impermeable for further comparison with numerical simulations. The formation of dissolution patterns and changes of fracture aperture due to the reactive-fluid percolation are monitored versus time using a numerical camera with a standard Charge Coupled Device (CCD) detector consisting of 3888×2592 pixels. The flow cell is illuminated by a source of homogeneous light located behind the experimental model and data processing is executed from the raw images recorded. Thus, transient changes in fracture aperture have been measured and analyzed for three representative cross sections, respectively, at z = 1.0 cm above the inlet, at the middle section (z = 5.0 cm), and z = 9.0 cm (i.e., at 1.0 cm below the outlet).

[6] On the basis of visual observations, two main configurations were detected depending on the flow rate (Figure 2):

2.1. Buoyancy-Dominated Dissolution (Experiment 1)

[7] The first regime is presented in Figures 2a–2c and is obtained for a low flow rate ($Q_v = 1.0$ mL/h). For this alteration pattern, dissolution occurs mainly in the upper part of the fracture leading to a change of walls shape. In the first approach, this behavior suggests that [*Dijk and Berkowitz*, 2000; *Dijk et al*., 2002]: (1) the chemical reaction rate at the wall surface is fast relative to reactant transport and (2) fracture dissolution results from buoyant convection. In other words: (1) the Damköhler number (*Da*) is sufficiently high to generate free convection and (2) buoyancy forces derived from the density contrast between injected and ambient fluids are dominant over forced convection. This experiment is in agreement with the study conducted by *Dijk et al*. [2002] on natural rock fractures and with the observed pattern that they obtained for a vertical orientation, referred to as *buoyancy-driven dissolution*. The transient variations of fracture aperture for different cross sections (Figure 3a) give a new insight on the physical mechanisms involved. Here, the fracture aperture at time t is divided by its initial value, i.e., 0.3 cm while the dimensionless time is the ratio between the measurement time t and the duration of each experiment. Observations indicate that the dissolution rate: (1) increases with the fracture elevation and (2) is practically uniform through time for each section. These measurements suggest flow stratification along the fracture elevation induced by the development of two counter-rotating cells, symmetric relative to the vertical axis. Beyond a period of transition (Figure 2a, $t < 10$ h), this density-stratification reaches a pseudo-stationary state (at least up to a certain extent of the fracture) which stabilizes the flow, and dissolution rate remains constant per cross section (Figure 3a).

2.2. Convection-Dominated Dissolution (Experiment 2)

[8] The second regime appears when the injection flow rate increases (Figures 2d–2e with $Q_v = 15$ mL/h). Uniform dissolution occurs, revealing a symmetric evolution of the fracture in accordance with the vertical axis that coincides with the flow direction. This behavior suggests that the dissolution regime is, this time, dominated by forced convection. Due to high injection rates, the forced flow reduces density gradients throughout the fracture and leads practically to a uniform constant concentration at the fluid/rock interface.

[9] Before concluding this experimental part, two experimental hurdles that had to be overcome are worth mentioning. First, the analysis of our experimental results

highlighted the emergence and the development of air bubbles arising from degassing during the dissolution of the rock matrix (they are particularly visible for $Q_v = 1.0$ mL/h in Figure 2). Despite our efforts to fully saturate the salt blocks with a preliminary step of vacuum degassing or CO_2 injection for flushing the air, this degassing phenomenon was permanently observed. Second, at long times, the fracture dissolution has exhibited the formation of lateral wormholes due to rock heterogeneity. As a consequence, we limited the duration of each experiment to minimize this effect in our analysis.

[10] However, the reproducibility of the experiments has been checked and is found to be quite good as illustrated by the results in Figure 3 where we have reported the fracture aperture versus time for these experiments repeated twice. Indeed, whatever the considered section, the maximum relative error defined as $(b_1 - b_2)/b_1$, where "b_i" is the fracture aperture for the experiment "i", is lower than about 15%. The good reproducibility of these experiments suggests a weak impact of the above-mentioned experimental issues on the resulting dissolution pattern.

3. Pore-Scale Equations

[11] Numerical simulations have been carried out in order to investigate further mechanisms that drive the dissolution in fracture in the presence of density contrasts. Moreover, the additional insight gained into physical processes involved, and the resulting complex dissolution patterns will be used for a comparison, at least qualitative, with the experiments. Conventionally, we denote by β the fluid phase percolating through the vertical fracture of initial aperture b and length l and by σ the rock matrix. We also assume that: (1) the fracture walls are impermeable, which is in agreement with the experimental observations and (2) the chemical reaction at the fluid-rock interface $A_{\beta\sigma}$ follows first-order kinetics. Moreover, we consider that the local fluctuations of solute concentrations in the fluid phase may be significant so that the reactant (or dissolved rock) transport in water may change the liquid density ρ_β. On the contrary, viscosity variations are ignored. Under these assumptions, the flow velocity cannot be solved independently from the reaction-transport problem, and the set of balance equations for mass, momentum, and species are expressed as:

$$\frac{\partial \rho_\beta}{\partial t} + \nabla\cdot\left(\rho_\beta \mathbf{v}_\beta\right) = 0 \tag{1}$$

$$\rho_\beta\left[\frac{\partial \mathbf{v}_\beta}{\partial t} + \mathbf{v}_\beta\cdot\nabla\left(\mathbf{v}_\beta\right)\right] = \rho_\beta \mathbf{g} - \nabla p_\beta + \mu_\beta \nabla^2 \mathbf{v}_\beta \tag{2}$$

$$\frac{\partial\left(\rho_\beta \omega_{A\beta}\right)}{\partial t} + \nabla\cdot\left(\mathbf{v}\,\rho_\beta \omega_{A\beta}\right) - \nabla\cdot\left[\rho_\beta D_m \nabla\left(\omega_{A\beta}\right)\right] = 0 \tag{3}$$

where $\omega_{A\beta}$ is the mass fraction of the dissolved species A (i.e., ω_{NaCl} in our case). These pore-scale equations call for boundary conditions, B.C. 1 and B.C. 2, at the fluid-rock interface $A_{\beta\sigma}$. Following the development proposed by *Luo et al*. [2012] for a binary (e.g., water-salt) system, the mass balance equations at the interface leads to the following relation:

$$\text{B.C.1} \qquad \mathbf{n}_{\beta\sigma}.\mathbf{w} = \mathbf{n}_{\beta\sigma}.\left(\frac{\Gamma \rho_\beta}{\rho_\sigma\left(1-\omega_{A\beta}\right)} D_{A\beta}\nabla\omega_{A\beta}\right) \quad \text{at } A_{\beta\sigma} \tag{4}$$

where $\mathbf{w}\cdot\mathbf{n}_{\beta\sigma}$ is the normal velocity of the fracture walls induced by dissolution. The equality between the total mass flux through $A_{\beta\sigma}$ and the reaction rate at the liquid-solid interface closes the system [*Fogler*, 1999] and assuming the first-order kinetics, we obtain:

$$\text{B.C.2} \qquad -\rho_\beta\left(\mathbf{v}_{A\beta} - \mathbf{w}\right)\cdot\mathbf{n}_{\beta\sigma} = \rho_\beta k_c\,\omega_{A\beta} \quad \text{at} A_{\beta\sigma} \tag{5}$$

with $\mathbf{v}_{A\beta}$ the velocity of the species A in the fluid phase.

[12] At this point, a complex coupling is involved between fluid flow and species transport due to fluid density variations. In order to reduce the degree of complexity of such a problem, we will use here the so-called Boussinesq approximation which states that the local fluctuations of the density can be neglected except in the gravity-dependent term. This approximation requires that density differences are sufficiently small compared to the reference density of the fluid (i.e., density of pure water) to be neglected. Classically, for transient problems, a limit of 1% of variation is often cited [*Bouquain et al*., 2011] but some studies [e.g., *Leijnse*, 1989; *Kolditz et al*., 1998] have found that, for steady state problems, some higher contrasts (for Elder problem, for instance, up to 10% of the reference value) did not necessarily lead to significant errors. As in our case, the density contrast may locally reach up to 25% (for carbonate systems, the maximum variation is around of 1%), the use of the Boussinesq approximation could be questionable and have an influence on the development and the symmetry of the counter-rotating cells [*Lee and Kim*, 2012]. On the other hand, due to the strong mixing within the fracture, it is obvious that, in the vicinity of the fluid-solid interface, the density gradient is significantly lower and, consequently, such an assumption could be consistent. Anyway, we assume this condition as valid for the problem studied here in the first approximation. In addition, we assume that the fluid density depends only on the local solute concentration:

$$\begin{aligned}\rho_\beta &= \rho_0\left(1 + \varepsilon\,\Delta\omega_{A\beta}\right) \text{ with } \varepsilon = \frac{1}{\rho_0}\frac{\partial \rho_\beta}{\partial \omega_{A\beta}} \\ &= \frac{1}{\rho_0}\frac{\rho_{\mathrm{sat}} - \rho_0}{\left(\omega_{\mathrm{sat}} - \omega_{\mathrm{inj}}\right)} \text{ and } \Delta\omega_{A\beta} = \omega_{A\beta} - \omega_{\mathrm{inj}}\end{aligned} \tag{6}$$

where ρ_0 is the density of the pure fluid, ρ_{sat} the saturated fluid density, ω_{sat} the mass fraction of saturated-brine solution in the liquid phase, and ω_{inj} the mass fraction of the injected undersaturated solution.

[13] Following a similar approach to that proposed by *Bouquain et al*. [2011], equations (1)–(3) become:

$$\nabla.\left(v_\beta\right) = 0 \tag{7}$$

$$\frac{\partial \mathbf{v}_\beta}{\partial t} + \mathbf{v}_\beta\cdot\nabla\left(\mathbf{v}_\beta\right) = -\varepsilon\rho_0\Delta\omega_{A\beta} g\nabla z - \nabla\left(\frac{p_\beta + \rho_0 g z}{\rho_0}\right) + \upsilon_{\beta 0}\nabla^2\mathbf{v}_\beta \tag{8}$$

$$\frac{\partial\left(\omega_{A\beta}\right)}{\partial t} + \nabla\cdot\left(\mathbf{v}_\beta\,\omega_{A\beta}\right) - \nabla\cdot\left(D_m\nabla\omega_{A\beta}\right) = 0 \tag{9}$$

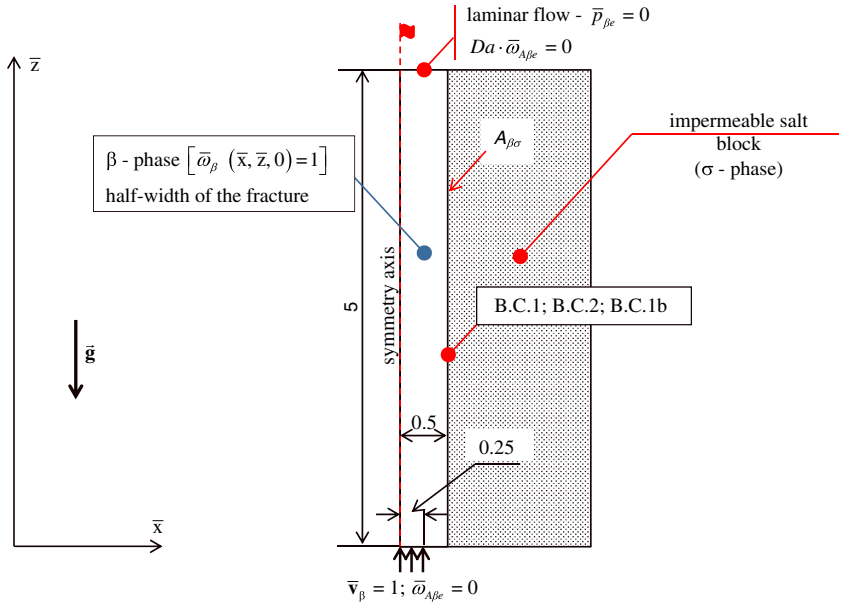

Figure 4. Geometry of the studied domain. Initial and boundary conditions are reported there.

where z is the space coordinate along the vertical direction and $\upsilon_{\beta 0} = \mu_\beta / \rho_0$ is the kinematic viscosity of pure water. Note that ρ_β is assumed to be constant (except in the gravity term) and consequently has been suppressed in equations (7)–(9). In addition, assuming that the mass fraction of the species A is negligible compared to one, i.e., $\omega_{A\beta} \ll 1$ (consistent with the Boussinesq approximation) and using a theory of diffusion [*Quintard and Whitaker*, 1999], the boundary conditions (4) and (5) can be simplified and we recover the relations derived for the tracer case [*Golfier et al.*, 2002]:

B.C.1 $$\mathbf{w} \cdot \mathbf{n}_{\beta\sigma} = \frac{\rho_\beta\, \Gamma\, D_m}{\rho_\sigma} \nabla \omega_{A\beta} \cdot \mathbf{n}_{\beta\sigma} \quad \text{at } A_{\beta\sigma} \tag{10}$$

B.C.2 $$D_m \nabla\left(\omega_{A\beta}\right) \cdot \mathbf{n}_{\beta\sigma} = k_c\, \omega_{A\beta} \quad \text{at } A_{\beta\sigma} \tag{11}$$

[14] Finally, if we assume that the dissolution rate $\mathbf{w}$ is slow enough (and not necessarily the reaction rate k_c, that is to say, it requires only that Γ is small enough) compared to the average flow velocity $\mathbf{v}_\beta$, then we have a quasi-steady assumption and a no-slip boundary condition that can be considered:

B.C.1b $$\mathbf{v}_\beta = 0 \quad \text{at } A_{\beta\sigma} \tag{12}$$

[15] Given the above assumptions, the final pore-scale boundary value problem can be written under a dimensionless form as follows:

$$\nabla . \left(\bar{\mathbf{v}}_\beta\right) = 0 \tag{13}$$

$$\frac{\partial \bar{\mathbf{v}}_\beta}{\partial \bar{t}} + \bar{\mathbf{v}}_\beta \cdot \bar{\nabla}\left(\bar{\mathbf{v}}_\beta\right) = -Ri \bar{\nabla} \bar{z} - \bar{\nabla} \bar{p}_\beta + Re^{-1} \bar{\nabla}^2 \bar{\mathbf{v}}_\beta \tag{14}$$

$$\frac{\partial \bar{\omega}_{A\beta}}{\partial \bar{t}} + \bar{\mathbf{v}}_\beta \cdot \bar{\nabla}\left(\bar{\omega}_{A\beta}\right) - \bar{\nabla} . \left[Pe^{-1} \bar{\nabla}\left(\bar{\omega}_{A\beta}\right)\right] = 0 \tag{15}$$

B.C.1 $$\bar{\mathbf{w}} \cdot \mathbf{n}_{\beta\sigma} = Pe^{-1} \cdot N_{\mathrm{ac}} \bar{\nabla}\left(\bar{\omega}_{A\beta}\right) \cdot \mathbf{n}_{\beta\sigma} \quad \text{at } A_{\beta\sigma} \tag{16}$$

B.C.1b $$\bar{\mathbf{v}}_\beta = 0 \quad \text{at } A_{\beta\sigma} \tag{17}$$

B.C.2 $$\bar{\nabla}\left(\bar{\omega}_{A\beta}\right) = Da\, \bar{\omega}_{A\beta} \quad \text{at } A_{\beta\sigma} \tag{18}$$

where the dimensionless quantities are given by,

$$\bar{x} = \frac{x}{b} \quad ; \quad \bar{z} = \frac{z}{b} \quad ; \quad \bar{t} = \frac{t\, v_{\mathrm{inj}}}{b}$$
$$\bar{\mathbf{v}}_\beta = \frac{\mathbf{v}_\beta}{v_{\mathrm{inj}}} \quad ; \quad \bar{p}_\beta = \frac{\left(p_\beta + \rho_0 g z\right)}{\rho_0 v_{\mathrm{inj}}^2} \quad ; \quad \bar{\omega}_{A\beta} = \frac{\omega_{A\beta}}{\omega_{\mathrm{sat}}} \tag{19}$$

and the dimensionless numbers are defined as follows:

$$Re_0 = \frac{b\, v_{\mathrm{inj}}}{\upsilon_{\beta 0}} \quad ; \quad Pe = \frac{b\, v_{\mathrm{inj}}}{D_m} \quad ; \quad Da = \frac{k_c\, b}{D_m} \quad ; \quad N_{\mathrm{ac}} = \frac{\rho_\beta\, \Gamma}{\rho_\sigma} \omega_{\mathrm{sat}}$$
$$Ri = \frac{\varepsilon\, \rho_0\, \Delta\omega_{A\beta}\, g\, b}{v_{\mathrm{inj}}^2} = \frac{\varepsilon\, \rho_0\, \Delta\omega_{A\beta}\, g\, b^3}{\upsilon_{\beta 0}^2} \frac{\upsilon_{\beta 0}^2}{b^2\, v_{\mathrm{inj}}^2} = Gr\, Re_0^{-2} \tag{20}$$

[16] The system is closed by the initial and boundary conditions applied on the external limits $A_{\beta e}$ of the domain. These conditions, presented in Figure 4, are expected to reproduce correctly the physical behaviors observed. First, Dirichlet boundary conditions on velocity and concentration were imposed only on a part of the inlet face (i.e., between $\bar{x} = 0$ and $\bar{x} = 0.25$) to be consistent with experimental conditions and maintain a constant injection velocity all along the fracture dissolution. At the outlet boundary, a far-field pressure condition is prescribed to maintain a laminar plug-flow far enough from the exit so that boundary conditions does not disturb the development of rotating recirculation zones. In a similar way, a zero-dispersive flux boundary condition is specified at the outlet for the transport equation.

[17] The Reynolds number Re_0 is classically low for the problem of interest to ensure a laminar flow regime, and the Acid capacity number N_{ac} represents the dissolving power of the reactant solution [*Golfier et al.*, 2002]. Both

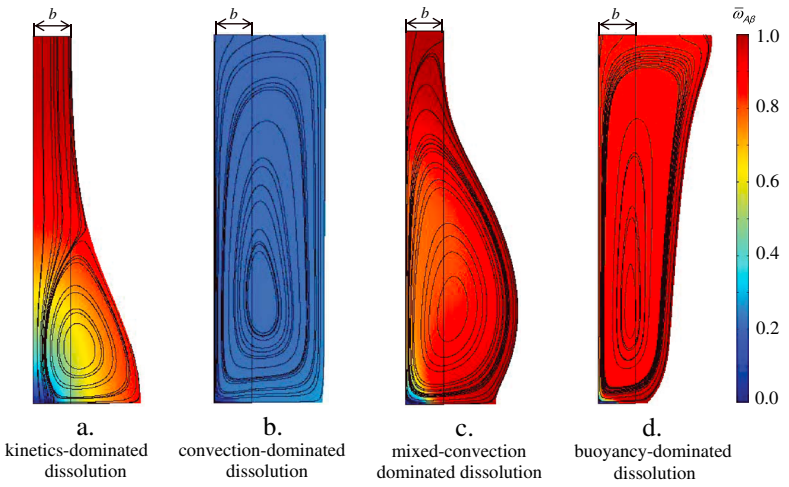

Figure 5. Example of numerical patterns of dissolution: (a) kinetics-dominated dissolution, $Pe = 2.0$, $Da = 2.0$, $Ri = 7.14 \times 10^2$; (b) convection-dominated dissolution, $Pe = 0.2$, $Da = 0.2$, $Ri = 7.14 \times 10^6$; (c) mixed-convection-dominated dissolution, $Pe = 0.2$, $Da = 200$, $Ri = 7.14 \times 10^4$; (d) buoyancy-dominated dissolution, $Pe = 0.2$, $Da = 200$, $Ri = 7.14 \times 10^6$.

dimensionless numbers have been kept constant for the rest of the simulations, i.e., $Re_0 = 0.2$ and $N_{ac} = 0.165$. We assumed a value of unity for the mass stoichiometric coefficient Γ and the density of the solid phase was set to 2170 kg/m^3. Let us remind that the Péclet number *Pe* quantifies the ratio between advection and diffusion processes while the Damköhler number *Da* is a measure of the relative importance of reaction kinetics over diffusion. The last dimensionless parameter involved is the so-called Richardson number *Ri*. Often used in thermal convection problems, the *Ri* number characterizes the importance of natural convection relative to forced convection. Note that an alternative formulation is to introduce the Grashof number *Gr* defined as the ratio of buoyancy forces to viscous forces.

4. Numerical Results—Discussions

[18] Under the limitations of the conceptual model above, the Péclet, Damköhler, and Richardson numbers are the only leading parameters driving the flow, solute transport, and dissolution within the system. As we said previously, *Re* and N_{ac} numbers have been fixed, and we have $Re = 0.2$ and $N_{ac} = 0.165$ that are consistent with a water-salt system. Therefore, all the simulations presented below will be given in terms of the three above-mentioned dimensionless parameters. The geometry of the numerical model, illustrated in Figure 4, is similar to the one of the experimental fracture. The domain of computation has been advantageously reduced by half using the vertical axis of symmetry. Note that the shape factor *F*, i.e., the ratio between the fracture length and its initial aperture, was set arbitrarily to 5 in our calculations to avoid meshing problems. This parameter was equal to 33 for the experiment. We expect a variation in terms of a displacement of the transition lines between the different dissolution regimes (see a discussion in *Golfier et al*., 2002 about these aspects) but the alteration patterns simulated should not be significantly modified by this discrepancy. The set of equations (13)–(18) was solved using the COMSOL Multiphysics Software ®. The main numerical difficulty comes from the coupling between fluid flow and buoyancy-driven solute transport in time-dependent domains. An Arbitrary Lagrangian Eulerian (ALE) method is used for addressing this issue and modeling dissolution walls. It is beyond the objective of this paper to discuss thoroughly the advantages and disadvantages of such a numerical approach as opposed to other solutions (e.g., diffuse interface methods, level set method, and volume of fluid method). Some comments on the use of this method can be found in the work of *Luo et al*. [2012]. We would just like to specify that this method on moving meshes is particularly appropriate to track the motion of the fluid-solid interface in time and recovering accurate values of the fluxes at walls. To assess the convergence of the solution, numerical simulations were stopped when the minimum mesh quality was lower than 0.1 for $Pe \leq 20$ and 0.01 for $20 \leq Pe \leq 200$. Then, data were saved, the deformed domain was remeshed and the computation was restarted. A convergence analysis has confirmed the grid-independence of the results. Numerical solutions were stopped as soon as the fracture aperture locally increased by a factor three.

[19] Simulations were performed over a wide range of Péclet, Damköhler, and Richardson numbers. Péclet and Damkhöler numbers vary between 2.0×10^{-1} and 2.0×10^2 while the Richardson number ranges from 7.14×10^2 to 7.14×10^6. This series of calculations have exhibited four representative dissolution patterns described as follows:

[20] 1. Kinetics-dominated dissolution (Figure 5a): Dissolution occurs mainly in the lower part of the fracture with a non-uniform increase of the aperture close to the injection inlet. This kind of dissolution pattern is classically observed in the absence of buoyancy effects when the Damköhler number is very high [*Békri et al*., 1997]. If Figure 5a evidences the presence of large concentration gradients in the vicinity of the inlet, the buoyancy-driven flow is not completely lacking, however. Convection cells appear but they are limited to the lower part of the fracture due to low values of the Richardson number. Note that *Chaudhuri et al.* [2009] have proposed a modified Rayleigh number criterion to determine the onset

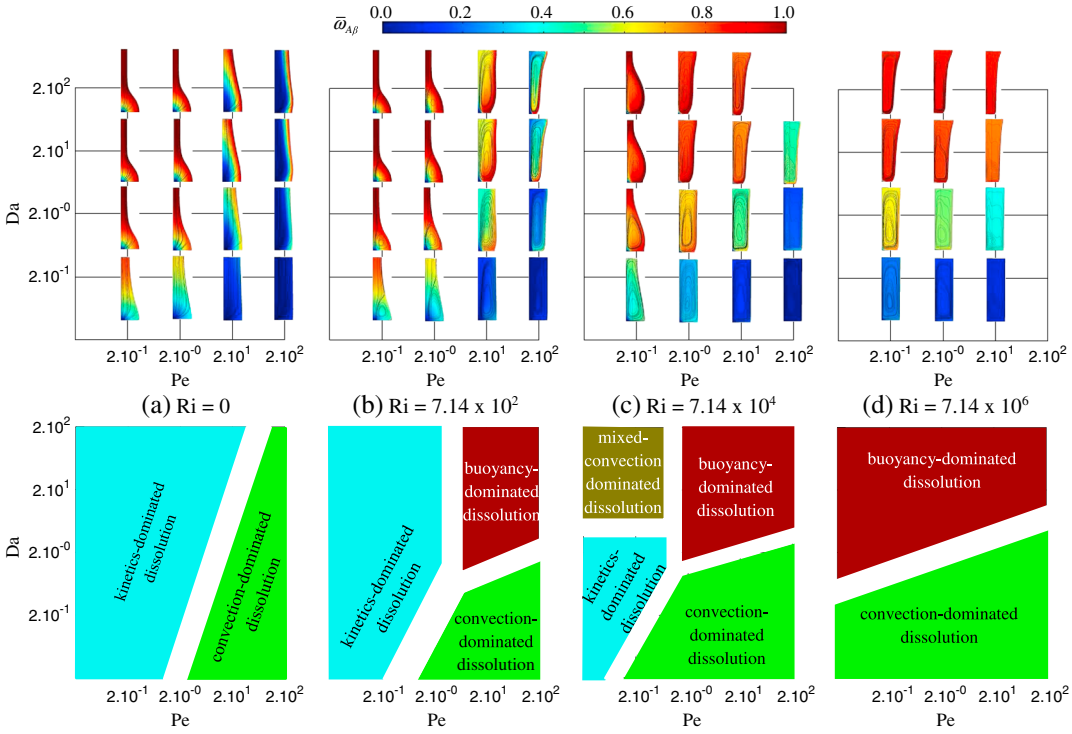

Figure 6. Numerical patterns of dissolution as a function of the Damköhler and Péclet numbers and empirical classification of dissolution regimes for: (a) $Ri = 0$ (tracer case); (b) $Ri = 7.14 \times 10^2$; (c) $Ri = 7.14 \times 10^4$; and (d) $Ri = 7.14 \times 10^6$.

of the instabilities resulting from the dissolution in vertical limestone fractures. However, such a criterion failed when applied to our calculations. This analysis confirms the complexity of the coupling involved and the impracticability of characterizing the onset of convective cells through a unique parameter.

[21] 2. Convection-dominated dissolution (Figure 5b): When the injection rate increases, dissolution becomes

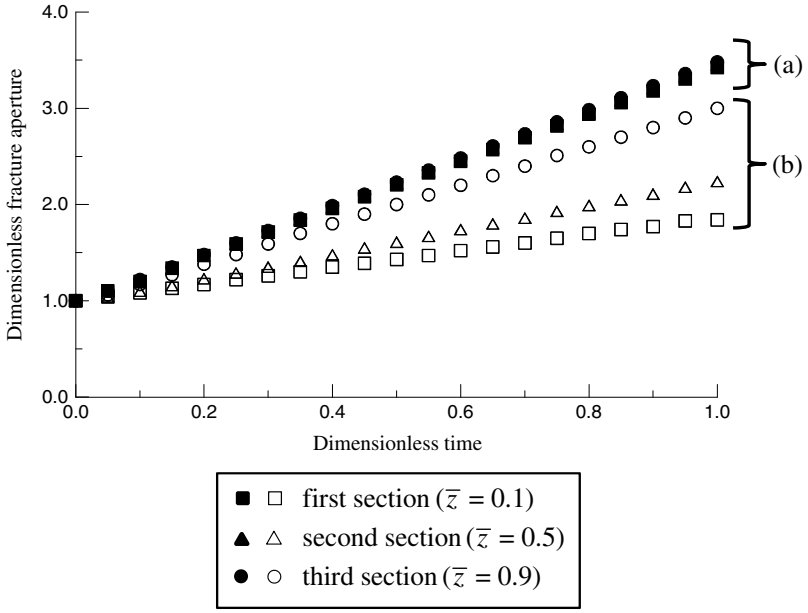

Figure 7. Evolution of the dimensionless fracture aperture versus time along three perpendicular sections to the mean flow for two numerical patterns of dissolution: (a) mixed-convection dominated dissolution, $Pe = 0.2$, $Da = 0.2$, $Ri = 7.14 \times 10^6$; (b) buoyancy dominated dissolution, $Pe = 0.2$, $Da = 2 \times 10^2$, $Ri = 7.14 \times 10^6$.

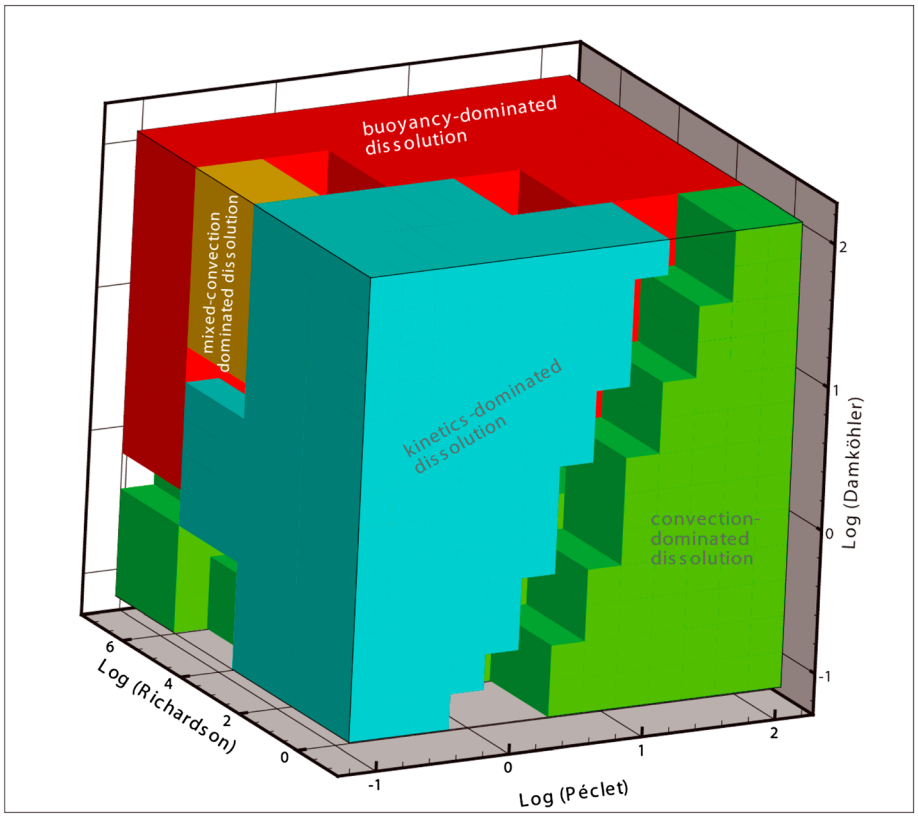

Figure 8. 3-D behavior diagram of the dissolution patterns.

uniform all along the fracture. Forced or mixed convection prevails and enhances a homogeneous mixing through the fracture. In other words, concentration gradients are quasi-constant per cross section. This alteration pattern is in agreement with experimental observations obtained with the salt fracture (see Figures 2d–2f).

[22] 3. Mixed-convection dominated dissolution (Figure 5c): For intermediate values of Richardson and Péclet numbers and high Damkhöler numbers, a transition regime is observed. Convective transport is here quite perfectly balanced by buoyancy effects and dissolution occurs preferentially in the middle part of the fracture. This very narrow regime is probably particularly sensitive to the value of the shape factor.

[23] 4. Buoyancy-dominated dissolution (Figure 5d): Finally, for high density contrasts, we recover the second regime observed experimentally (see Figures 2a–2c). Dissolution is now driven mainly by buoyancy forces and the fracture alteration increases upward.

[24] In order to obtain a better insight of how the physical mechanisms involved (free and forced convection, reaction kinetics) may affect the dissolution process and consequently the resulting fracture patterns, we have represented these four different configurations in a *Pe-Da* diagram for a fixed *Ri* number. Resulting diagrams in a log-log representation are illustrated in Figure 6 for respectively $Ri = 0$ (tracer case), $Ri = 7.14 \times 10^2$, $Ri = 7.14 \times 10^4$, and $Ri = 7.14 \times 10^6$:

[25] 1. For $Ri = 0$ (Figure 6a), two patterns only are observed, and we recover the classical dissolution diagram in the absence of buoyancy [*Békri et al.*, 1997; *Detwiler and Rajaram*, 2007]. For $Pe \gg Da$, a convection-dominated dissolution regime is obtained; while under high Damköhler, fracture patterns are characterized by kinetics-dominated dissolution. This good agreement with the results of *Békri et al.* [1997] and *Dijk and Berkowitz* [1998] confirms the viability of our model.

[26] 2. For low Richardson numbers ($Ri = 7.14 \times 10^2$, Figure 6b), we obtain at first sight a diagram similar to the previous one. For low and intermediate *Pe* and *Da* values, the same configurations, respectively kinetics- and convection-dominated dissolution patterns, are observed. However, a more careful investigation of streamlines indicates the presence of convection rolls for both patterns. For dominant Damköhler numbers, the pair of rolls is located only on the lower part of the domain and grows as the fracture widens since the critical Richardson number is not reached everywhere. On the contrary, for dominant Péclet numbers, convective cells occupy all the fracture space. A uniform dissolution is still observed but the homogeneous mixing is driven now by mixed convection. It should be specified, however, that the onset of convective rolls is largely enhanced by the mode of injection (the same simulations for $Da = 0.2$ with an injection distributed all over the inlet face do not exhibit these rolls). Finally, for high Péclet and Damköhler, this similarity with the tracer case disappears. With the increase of density contrast, free convection prevails and an upward gradient of dissolution begins to form (buoyancy-dominated dissolution).

[27] 3. For the intermediate values of the Richardson number ($Ri = 7.14 \times 10^4$, Figure 6c), buoyancy forces

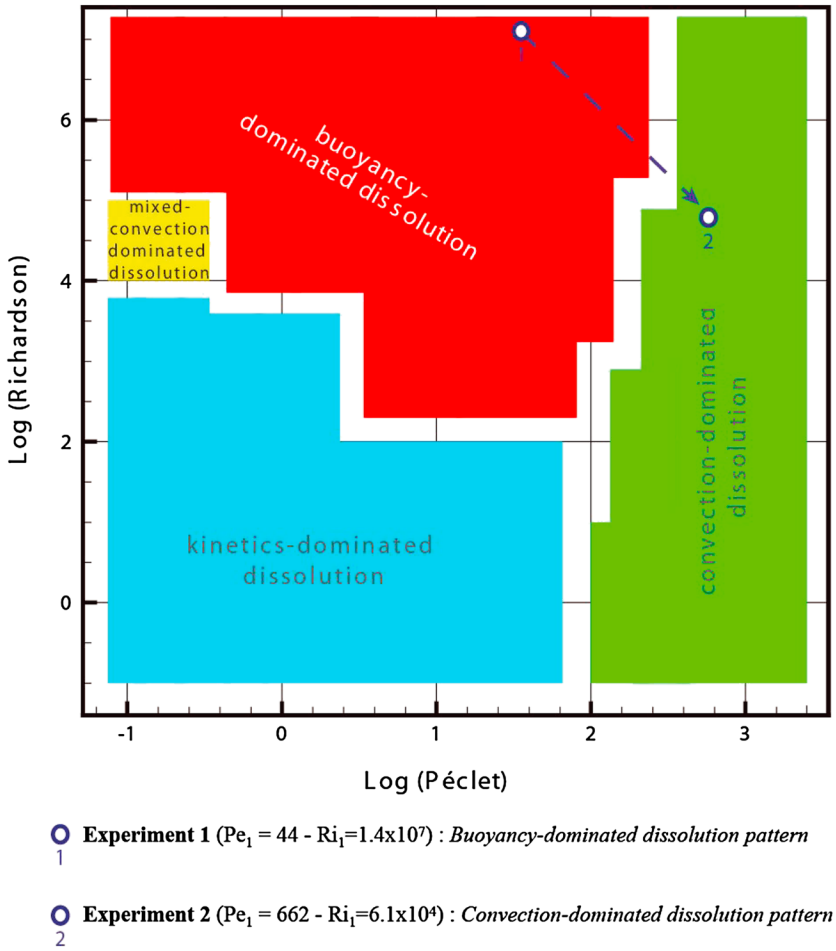

Figure 9. Plot illustrating the empirically-classified dissolution regimes for the estimated value of the experimental Damkhöler number ($Da = 4$). The points 1 and 2 correspond to the experiments conducted in this paper.

increase and convective rolls are found to occupy the full height of the fracture except for very low *Da*. As a consequence, the kinetics-dominated dissolution regime is significantly reduced with an apparent displacement from the right to the left of convection- and buoyancy-dominated regimes. In addition, a new dissolution pattern is obtained for high *Da* and low *Pe* values. At constant Péclet number, indeed, a transition from kinetics-dominated to mixed-convection-dominated dissolution regime is observed. As *Da* increases, buoyant flow becomes significant and causes the alteration zone to move upward. The relative magnitude of both forces (buoyancy and chemical reaction) drives the exact location of the zone of dissolution. In other words, this regime can be seen as a transition regime between kinetics-dominated and buoyancy-dominated dissolution patterns.

[28] 4. Finally, for very high *Ri* values ($Ri = 7.14 \times 10^6$, Figure 6d), buoyancy forces are strictly dominant relative to the reaction kinetics (at least, over the range of *Da* investigated) and only the competition with the forced convection remains. In such conditions, two dissolution patterns merely subsist, respectively the convection-dominated and buoyancy-dominated regimes. For these last two configurations (i.e., $Pe = 0.2$, $Da = 0.2$ and $Da = 200$), we also analyzed the transient variation of fracture aperture for different cross sections (Figure 7). The numerical results present, as the experimental observation, the same behavior. From Equation (16) describing the velocity of the fluid-rock interface, we may conclude that concentration gradients remain constant in the vicinity of the fracture walls after the onset of convective cells.

[29] We plotted the 3-D behavior diagram in Figure 8 to provide a general overview of the interaction between buoyancy, fluid injection, and reaction kinetics and make an assessment of their impact on dissolution patterns. Richardson number values range from $Ri = 10^0$ (similar to the case without buoyancy effects, i.e., $Ri = 0$) to $Ri = 10^7$ and boundaries separating the different regimes were obtained using linear interpolation. The diagram reveals clearly the transition between the different dissolution regimes whatever the values of the different parameters. Additionally, this figure helps gaining an insight into the experimental behavior observed. Thus, in the present study, we moved from the buoyancy-dominated (Figures 2a–2c, experiment 1: $Pe_1 = 44$, $Ri_1 = 1.4 \times 10^7$) to the convection-dominated dissolution pattern (Figures 2d–2f, experiment 2: $Pe_2 = 662$, $Ri_2 = 6.1 \times 10^4$) at a constant

Damköhler number. Although the exact value of the salt dissolution kinetics rate is unknown, it is usually considered that the dissolution process of salt is mass-transfer limited [*Golfier et al*., 2002] and, therefore, that the constant rate is very high. The usual values found in the literature for halite dissolution rate are around $k_c \approx 2-4\ 10^{-6}\ \mathrm{ms}^{-1}$ [*Stiller et al*., 2007; *Weisbrod et al*., 2012]. Therefore, we will consider for the rest of the analysis a *Da* value of 4. This is not a restrictive and major assumption since we could pursue the same method and obtain a similar qualitative interpretation with higher Damköhler values. A cross-section along the plane $Da = 4$ was extracted, and we carried out further simulations for Péclet numbers beyond 200 to proceed with this analysis, as illustrated in Figure 9. The experiments that we have conducted are also indicated and numerical predictions are in agreement with experimental evidence, given the numerical uncertainties (estimate of the Damköhler number, the discrepancy between experimental and numerical values of the shape factor, the empirically-defined boundaries of dissolution regimes). Although purely qualitative, this comparison with the model explains the existence of only two observable experimental patterns at high *Da* numbers as emphasized also by *Dijk and Berkowitz* [2000] and indicates how the fracture dissolution may be affected by changes of injection conditions.

5. Conclusions

[30] In this paper, we investigated the changes of geometrical patterns induced by dissolution for a vertical fracture. Experimental observations suggest a strong coupling between buoyancy effects, convective transport, and kinetics reactions. When the dissolution is dominated by buoyant convection (experiment 1), the resulting fracture evolution is characterized by an upward dissolution, in agreement with the experimental results of *Dijk et al*. [2002]. On the contrary, if the dissolution is driven by forced convection (experiment 2), a quasi-constant aperture variation along the fracture height was observed.

[31] Numerical simulations have been conducted for a broad range of the characteristic dimensionless numbers of the process, i.e., the Richardson, Damköhler, and Péclet numbers. Results indicate quite a good qualitative agreement with the experimental study and highlight the complexity of coupling between the different physical mechanisms involved. A 3-D behavior diagram was constructed from these simulations, and the four empirically-classified dissolution regimes can be detailed as follows:

[32] 1. For high *Pe* and low *Da* values, an almost uniform enlargement of fractures is observed. This dissolution pattern, similar to experiment 2, corresponds to a regime dominated by convection.

[33] 2. For low *Ri* and low *Pe* values, dissolution occurs early in the vicinity of the inlet. Here, morphological changes in fractures are mainly driven by kinetics reaction. This configuration has not been observed experimentally.

[34] 3. For low *Pe*, high *Da*, and moderate *Ri* values, the dissolution process causes a local non-uniform enlargement of the fracture. This alteration pattern can be seen as a transitionary regime, a globally unstable equilibrium state resulting from a balance between the different mechanisms involved.

[35] 4. For high *Da*, moderate *Pe*, and moderate to high *Ri* values, buoyancy forces become important, and we recover the experimental behavior at large flow rates (experiment 1). For given *Pe* and *Ri* values, an increase of the Damköhler number speed up the dissolution of the upper part of the fracture.

[36] These results indicate that gravity play a key role in fracture dissolution in evaporite formations and may enhance dissolution upwards. It should have a great impact on sinkhole formation for instance. Ultimately, although this paper provides additional insight into buoyancy-driven dissolution, it also supports the conclusions by *Dijk et al*. [2002] that state that "the coupled flow and dissolution processes are much more complex and unpredictable than commonly assumed, even under simplified conditions". However, an application of these results to the field-scale conditions is not straightforward. Changes of fracture morphology due to variation of local aperture or to wall roughness have not been considered in this study and should significantly modify the dissolution patterns (e.g., formation of preferential dissolution zones), as emphasized by *Dijk et al*. [2002]. The impact of the fracture size, as expressed through the shape factor *F*, is another question that remains unanswered and will deserve further study. Investigation has been made for a fracture of finite length but would a dissolution pattern dominated by buoyancy still exist for an infinite-length fault or at least with a very high shape factor? Therefore, such a study calls for new laboratory experiments to extend the range of operating conditions (injection flow rate, concentration, and shape factor) and configurations (horizontal fracture and downward injection) of interest. A further investigation based on non-intrusive methods (e.g., PIV and Background Oriented Schlieren method for velocity and concentration measurements) will also be required to characterize the onset of buoyancy convection.

Notation

$A_{\beta\sigma}$	solid-rock interface
b	fracture aperture [L]
β	fluid phase [−]
C_{sat}	concentration of saturated-brine solution [ML^{-3}]
C_{inj}	injection concentration of undersaturated solution [ML^{-3}]
D_m	solute molecular diffusivity [$\mathrm{L}^2\mathrm{T}^{-1}$]
$Da = \frac{k_c\, b}{D_m}$	Damköhler number [−]
$\mathbf{g}$	gravity vector [LT^{-2}]
Γ	mass stoichiometric coefficient of the chemical reaction [−]
k_c	reaction rate constant [MT^{-1}]
μ_β	fluid dynamic viscosity [$\mathrm{ML}^{-1}\mathrm{T}^{-1}$]
$\nu_{\beta 0}$	fluid kinematic viscosity [$\mathrm{L}^2\mathrm{T}^{-1}$]
$\mathbf{n}_{\beta\sigma}$	unit normal vector to the β-σ surface [−]
$N_{\mathrm{ac}} = \frac{\rho_{\mathrm{sat}}\,\Gamma}{\rho_\sigma}\omega_{\mathrm{sat}}$	Acid capacity number [−]
$Pe = \frac{b\, v_{\mathrm{inj}}}{D_m}$	Péclet number [−]
p_β	pressure in the fluid phase [$\mathrm{ML}^{-1}\mathrm{T}^{-2}$]
$\bar{p}_\beta = \frac{p_\beta + \rho_0 g z}{\rho_0 v_{\mathrm{inj}}^2}$	dimensionless pressure [−]

Q_v injection flow rate [L^3T^{-1}]

$Re_0 = \frac{b\, v_{inj}}{\nu_{\beta 0}}$ Reynolds number [−]

$Ri = \frac{\varepsilon\, \rho_0\, \Delta\omega_{A\beta}\, g\, b}{v_{inj}^2}$ Richardson number [−]

ρ_β liquid density [ML^{-3}]

ρ_σ rock density [ML^{-3}]

σ solid phase [−]

t time [T]

$\bar{t} = \frac{t\, v_{inj}}{b}$ dimensionless time [−]

$\mathbf{v}_\beta$ β- phase velocity [LT^{-1}]

$\mathbf{v}_\sigma$ σ- phase velocity [LT^{-1}]

$\bar{v}_\beta = \frac{\mathbf{v}_\beta}{v_{inj}}$ dimensionless pore-fluid velocity [−]

v_{inj} injection vertical velocity [LT^{-1}]

$\omega_{A\beta}$ mass fraction of the species "A" [MM^{-1}]

$\bar{\omega}_{A\beta} = \frac{\omega_{A\beta}}{\omega_{sat}}$ dimensionless mass fraction of the species "A" [−]

ω_{sat} mass fraction of saturated-brine solution [MM^{-1}]

ω_{inj} mass fraction of the injected undersaturated solution [MM^{-1}]

w velocity of the fracture walls [LT^{-1}]

[37] **Acknowledgments.** This work was partially supported by the French National Research Agency through the national program "Investissements d'avenir" with the reference ANR-10-LABEX-21-RESSOURCES21 and by the French Scientific Interest Group-Industrial Wasteland (GISFI) program.

References

Alkattan, M., E. H. Oelkers, J. L. Dandurand, and J. Schott (1997), Experimental studies of halite dissolution kinetics. 1. The effect of saturation state and the presence of trace metals, *Chem. Geol.*, *137*, 201–219.

Anderson, R. Y., and D. W. Kirkland (1980), Dissolution of salt deposits by brine density flow, *Geology*, *8*, 66–69.

Békri, S., J.-F. Thovert, and P. M. Adler (1997), Dissolution and deposition in fractures, *Eng. Geol.*, *48*, 283–308.

Berkowitz, B. (2002), Characterizing flow and transport in fractured geological media: A review, *Adv. Water Resour.*, *25*, 864–884.

Berkowitz, B., and J. Zhou (1996), Reactive solute transport in a single fracture, *Water Resour. Res.*, *32*, 901–913.

Bouquain, J., Y. Meheust, and P. Davy (2011), Horizontal pre-asymptotic solute transport in a plane fracture with significant density contrasts, *J. Contam. Hydrol.*, *120–121*, 184–197. doi:10.1016/j.jconhyd.2010.08.002.

Chaudhuri, A., H. Rajaram, H. Viswanathan, G. Zyvoloski, and P. Stauffer (2009), Buoyant convection resulting from dissolution and permeability growth in vertical limestone fractures, *Geophys. Res. Lett.*, *36*, L03401, doi:10.1029/2008GL036533.

Detwiler, R. J. (2008), Experimental observations of deformation caused by mineral dissolution in variable-aperture fractures, *J. Geophys. Res.*, *113*, B08202, doi:10.1029/2008JB005697.

Detwiler, R. L., and H. Rajaram (2007), Predicting dissolution patterns in variable aperture fractures: Evaluation of an enhanced depth-averaged computational model, *Water Resour. Res.*, *43*, W04403, doi:10.1029/2006WR005147.

Detwiler, R. L., R. J. Glass, and W. L. Bourcier (2003), Experimental observations of fracture dissolution: The role of Peclet number on evolving aperture variability, *Geophys. Res. Lett.*, *30*(12), 1648, doi:10.1029/2003GL017396.

Dijk, P. E., and B. Berkowitz (1998), Precipitation and dissolution of reactive solute in fracture, *Water Resour. Res.*, *34*, 457–470.

Dijk, P. E., and B. Berkowitz (2000), Buoyancy-driven dissolution enhancement in rock fractures, *Geol.*, *28*(11), 1051–1054.

Dijk, P. E., B. Berkowitz, and Y. Yechieli (2002), Measurement and analysis of dissolution patterns in rock fractures, *Water Res. Resour.*, *38*(2), doi:10.1029/2001WR000246.

Fogler, H. S. (1999), *Elements of Chemical Reaction Engineering*, 3rd ed., Prentice-Hall PTR, Upper Saddle River, N.J.

Fredd, C. N., and M. J., Miller (2000), Validation of carbonate matrix simulation models, paper presented at the International Symposium on Formation Damage Control, Lafayette, Louisiana, USA, doi:10.218/58713-MS.

Golfier, F., C. Zarcone, B. Bazin, R. Lenormand, D. Lasseux, and M. Quintard (2002), Modelling of the dissolution in porous media at the Darcy-scale: On the ability of a Darcy-scale model to capture wormhole formation during the dissolution of a porous media, *J. Fluid Mech.*, *457*, 213–254.

Hoefner, M. L., and H. S. Fogler (1988), Pore evolution and channel formation during flow and reaction in porous media, *AICHE J.*, *34*(1), 45–54.

Kang, Q., D. Zhang, and S. Chen (2003), Simulation of dissolution and precipitation in porous media, *J. Geophys. Res.*, *108*(B10), 2505, doi:10.1029/2003JB002504.

Kolditz, O., R. Ratke, H.-J. G. Diersch, and W. Zielke (1998), Coupled groundwater flow and transport: 1. Verification of variable density flow and transport models, *Adv. Water Res.*, *21*(1), 27–46.

Lee, H. G., and J. Kim (2012), A comparison study of the Boussinesq and the variable density models on buoyancy-driven flows, *J. Eng. Math.*, *75*(1), 15–27, doi:10.1007/s10665-011-9504-2.

Leijnse, T. (1989), Free convection for high concentration solute transport in porous medium, in *Contaminant Transport in Groundwater*, edited by H. E. Kobus and W. Kinzelbach, pp. 341–346, A. A. Balkema, Rotterdam/Brookfield.

Luo, H., M. Quintard, G. Debenest, and F. Laouafa (2012), Properties of a diffuse interface model based on a porous media theory for solid-liquid dissolution problem, *Comput. Geosci.*, *16*, 913–932, doi:10.1007/s10596-012-9295-1.

Mainhagu, J., F. Golfier, C. Oltéan, and M. A. Buès (2012), Gravity-driven fingers in fractures: Experimental study and dispersion analysis by moment method for a point-source injection, *J. Cont. Hydro.*, *132*, 12–27.

van Noorden, T. (2009), Crystal Precipitation and Dissolution in a Porous Medium: Effective Equations and Numerical Experiments, *Multiscale Model. Simul.*, *7*(3), 1220–1236, doi:10.1137/080722096.

Quintard, M., and S. Whitaker (1999), Dissolution of an immobile phase during flow in porous media, *Ind. Eng. Chem. Res.*, *38*(3), 833–844, doi:10.1021/ie980212t.

Simmons, C. T., M. L. Pierini, and J. L. Hutson (2002), Laboratory investigation of variable-density flow and solute transport in unsaturated–saturated porous media, *Transport Porous Med.*, *47*, 215–244.

Stiller, M., Y. Yechieli, and I. Gavrieli (2007), The rate of dissolution of halite in diluted Dead Sea brines, *Rep. GSI/01/2007*, Isr. Geol. Surv., Jerusalem.

Szymczak, P., and A. J. C. Ladd (2009), Wormhole formation in dissolving fractures, *J. Geophys. Res.*, *114*, B06203, doi:10.1029/2008JB006122.

Szymczak, P., and A. J. C. Ladd (2012), Reactive-infiltration instabilities in rocks. Fracture dissolution, *J. Fluid Mech.*, *702*, 239–264, doi:10.1017/jfm.2012.174.

Weisbrod, N., C. Alon-Mordish, E. Konen, and Y. Yechieli (2012), Dynamic dissolution of halite rock during flow of diluted saline solutions, *Geophys. Res. Lett.*, *39*, L09404, doi:10.1029/2012GL051306.

Wooding, R. A., S. W. Tyler, and I. White (1997), Convection in groundwater below evaporating salt lake: 1. Onset of instability, *Water Resour. Res.*, *33*, 1199–1217.